Electrical/thermal behaviors of bimetallic (Ag-Cu, Ag-Sn) nanoparticles for the printed electronics

Electrical/thermal behaviors of bimetallic (Ag-Cu, Ag-Sn) nanoparticles for the printed electronics

Xin Wang[a†], Feirong Huang[a†], Dongxing Wang[b], Da Li[c], Pu Li[d], Javid Muhammad[a], Xinglong Dong[a*] and Zhidong Zhang[c]

[a]School of Materials Science and Engineering, Key Laboratory of Materials Modification by Laser, Ion and Electron Beams (Ministry of Education), Dalian University of Technology, Dalian 116023, P.R. China.

[b]Institute of Materials, Ningbo University of Technology, Ningbo, 315016, P.R. China.

[c]Shenyang National Laboratory for Materials Science, Institute of Metal Research, International Centre for Materials Physics, Chinese Academy of Sciences, Shenyang 110016, P.R. China.

[d]China United Test & Certification Co., LTD, General Research Institute for Nonferrous Metals, Beijing, 100088, P.R. China.

[†]These authors contributed equally to this work.

[*]E-mail address: dongxl@dlut.edu.cn (X. Dong).

Abstract

In this work, Ag-Cu and Ag-Sn nanoparticles (NPs) were synthesized by a physical vapor condensation method, i.e. DC arc-discharge plasma. The as-prepared bimetallic nanoparticles consist of metallic cores of Ag-Cu or Ag-Sn and ultrathin oxide shells of CuO or a hybrid of SnO and SnO_2. Ag-Sn NPs exhibit a room temperature resistivity of 4.24×10^{-5} Ω·cm, a little lower than 7.10×10^{-5} Ω·cm of Ag-Cu NPs. Both bimetallic nanoparticles demonstrate a typical metallic conduction behavior with a positive temperature coefficient of resistance (TCR) over 25-300 K. Ag-Sn NPs exhibit thermally competitive stability up to 230 °C and a lower resistivity of 3.18×10^{-5} Ω·cm after sintering at 200 °C, making it potential for the flexible printed electronics.

Keywords

DC arc-discharge method, bimetallic nanoparticles, printed electronics, thermal-stability, resistivity

1. Introduction

In recent years, tremendous attention has been devoted to printed electronics behind the desirable impact on consumer electronics market that could be estimated as much as hundreds of billions of dollars over the next 10 years [1, 2]. Although conventional methods, *i.e.* photolithography, vacuum deposition and electroless plating processes, have been widely adopted in micro-fabrication of various electronic devices, these are subject to limitations of complexity, cost-effectiveness and environmental consideration, etc. [3, 4]. In this context, the direct digital printing techniques, such as inkjet printing and airbrush spraying, have garnered worldwide interest owing to the merits of simplicity, cheapness and eco-friendliness [5, 6], as well as their potential applications in transparent electrodes, radio frequency identification (RFID), thin film transistors, light emitting devices, solar cells, etc. [2, 7-9].

As conductive ink is a multi-component system comprising of a conducting material and various additives, much effort was paid to the synthesis of conductive materials and their applications. A number of nanomaterials including metal nanoparticles (NPs), carbon nanotubes (CNTs), graphene oxide (GO), conductive polymers (dissolved or dispersed) as well as organometallic compounds have contributed to the conductive materials for printed electronics [10-12]. Among them, the metal nanoparticles are considered the stunningly promising conductive materials with excellent electrical performances. Apparently, their best candidates are the metals with low electrical resistivity (ρ), such as Ag (1.59×10^{-6} Ω·cm), Cu (1.72×10^{-6} Ω·cm), Au (2.26×10^{-6} Ω·cm), Al (2.65×10^{-6} Ω·cm) and Sn (1.01×10^{-5} Ω·cm) [1, 11, 13, 14]. Up to date, most conductive materials in electronic devices are based on silver nanoparticles due to its lowest electrical resistivity and prominent ability against oxidation. In practice, pure silver nanoparticles are expensive due to the fact that silver has a high price, thus in some way hindering a wide application in the large-area printed electronics. On the other hand, silver is found subject to susceptibility of ion migration under relatively high temperature and humidity conditions [3]. In view of all these issues, to integrate alternative metals such as Cu or Sn with Ag is a worthy strategy for the fabrication of conductive materials for printed electronics. Ag-Sn NPs have manifested a cost-effective way for highly conductive materials, where the formation of Ag-rich phases of Ag_3Sn or Ag_4Sn can restrain the generation of β-Sn phase, raise the anti-oxidization ability as well as reduce the sintering temperature in following post-treatments [4]. It is also indicated that partial substitute of silver with copper element to improve the anti-

oxidization ability of Ag-Cu NPs is still a crucial challenge [4, 7, 13, 15, 16].

Although there are various techniques employed for the preparation of bimetallic nanoparticles, two main methods are reported for the synthesis of Ag-based bimetallic nanoparticles [1, 17]. The first one essentially requires the use of a reductant, while the second is based on a galvanic displacement reaction, *i.e.* transmetallation reaction. Chen et al. [18] reported air-stable Cu-Ag NPs prepared by alcohol reduction with the assistance of microwave irradiation. Jo et al. [4] demonstrated highly conductive Ag-Sn NPs through a polyol process with a reducing agent of $NaBH_4$. Lee et al. [10] synthesized the uniform core-shell Cu-Ag NPs using a facile two-step process of thermal decomposition and galvanic displacement methods.

Here we present a novel approach of physical vapor condensation, which is applied to synthesize Ag-Cu NPs and Ag-Sn NPs using DC arc-discharge plasma as the thermal source. This route demonstrated effective in the fabrication of various metal nanoparticles with many advantages of easy operation, controllable experiment condition, large-scale production, good dispersion and high purity. Excellent electrical/thermal performances of Ag-Cu NPs and Ag-Sn NPs in this work are convinced of new opportunities for the conductive patterns of printed electronics.

2. Material preparation and characterization

The details of DC arc-discharge plasma method have been well described in our publications [19-21]. Briefly, Ag-Cu NPs and Ag-Sn NPs were prepared by evaporation of bulk targets under a mixture atmosphere of hydrogen (H_2, 0.1×10^5 Pa) and argon (Ar, 0.1×10^5 Pa). The target was prepared by compressing micron-sized silver and copper (or tin) powders, which were first homogeneously mixed in a mass ratio of 1:1. To start production of the bimetallic nanoparticles, arc plasma was triggered between an anode (the target) and a tungsten rod cathode. Products were obtained through successive nucleation and growth processes, along with a passivation stage for 12 h after introducing a trace of air into the chamber. For electrical resistivity measurement, the testing samples were prepared by mechanically pressing pristine nanoparticles into thin sheets in a steel die under 20 MPa, which also suffered from a sintering treatment in a tube furnace at various temperatures (473, 573, 773 and 973 K) under Ar gas atmosphere for 1 h. The diameter of the thin sheets used here is 20 mm with a thickness of ~0.35 mm.

The crystal structures of the as-obtained nanoparticles were identified using X-ray diffraction

(XRD, Shimadzu X-ray 6000) operated at 40 kV and 30 mA with Cu Kα radiation (λ=1.5418 Å). The morphology and microstructures of the products were investigated by transmission electron microscopy (TEM, Tecnai^2 20 S-TWIM) with an accelerating voltage of 200 kV. The mean size and distribution of the nanoparticles were obtained by statistical analysis on TEM pictures. The lattice spacing of each phase in the nanoparticles was determined by HRTEM, which further confirms the detailed core-shell structure. Surface oxide species of the nanoparticles were investigated by X-ray photoelectron spectroscopy (XPS, Thermo Escalab 250Xi). Thermogravimetric analysis (TGA) and differential scanning calorimetry (DSC) were conducted by the simultaneous thermal analyzer (STA, 449 F3, Netzsch). The signal was recorded from 50 to 900 °C at a ramp rate of 10 °C min^{-1} under air atmosphere. The electrical resistivity of thin sheets and their annealed samples were measured by a four-probe resistance meter (Keithley 2400) fitted with Au tip electrodes. The temperature-dependent resistivity of testing sheets was also measured from 2 to 300 K on a physical property measurement system (PPMS, Quantum Design).

3. Results and discussions

Fig. 1 shows XRD patterns of the as-prepared bimetallic nanoparticles. It is found that Ag-Cu NPs (Fig. 1a) consist of two crystal phases. The Ag grains diffract at 2θ = 38.4°, 44.7°, 65.1° and 78.0°, which are indexed to (111), (200), (220) and (311) lattice planes of FCC Ag (JCPDS #87-0720), while the Cu phase is of FCC Cu (JCPDS #04-0836) with diffraction peaks at 2θ = 43.0°, 50.1° and 73.6° assigned to (111), (200) and (220) crystal planes, respectively. In comparison with the lattice constants of bulk Ag (4.077 Å) and Cu (3.616 Å), the calculated ones of the nanoparticles are $a_{(Ag)}$ = 4.0507 Å and $a_{(Cu)}$ = 3.640 Å, with a lattice constriction of about -0.67% for the Ag phase and a lattice expansion of 0.66% for the Cu phase. The variation of lattice constant implies the formation of solid solutions of Ag(Cu) and Cu(Ag) in the nanoparticles [22]. The atomic radii of Cu and Ag are 0.14 and 0.16 nm [23], respectively. A hard sphere model is adequately available here: since Cu is the smaller atom, the dissolution of Cu in the Ag matrix causes lattice contraction; but instead Ag incorporation into the Cu matrix creates lattice expansion. However, according to the equilibrium phase diagram of binary Ag-Cu alloy, any Ag-Cu intermetallic compound is not generated due to their weak chemical affinity. In Fig. 1(b), Ag-Sn NPs show two sets of diffraction profiles: the Ag_3Sn phase (JCPDS #71-0530) displays peaks at 2θ = 34.7°, 37.3°, 39.6° and 52.1°,

whereas the Sn phase (tetragonal in lattice cell, JCPDS #86-2264) illustrates the peaks at 2θ = 30.8°, 32.1°, 44.0° and 45.0°. It is noteworthy that the emergence of Ag_3Sn phase in the nanoparticles indicates an active reaction occurred between Ag and Sn elements, while the intermetallic compound product consumed all Ag content. The phase diagram concerning their nanoparticles' system also supports above results [24-26]. The formation of Ag-Sn intermetallic compounds will be achieved if the concentration of Sn is higher than 25 wt.%. Thus, it is believed that the composition of the raw materials (50 wt.% of Sn) has well satisfied the formation condition for the Ag_3Sn compound in the nanoparticles [4, 27]. Additionally, it had been confirmed in previous studies that the passivation process can result in oxide shells at the surface of metal nanoparticles [28]. However, the oxides species have not appeared in the XRD profiles owing to their amorphous states and/or being much thinner in thickness, or in a quantity less than 5 wt.%. The oxide shells will be easily determined by following TEM and XPS measurements. The average sizes of primary crystalline grains are calculated using the Scherrer equation [29]: $D(\text{nm}) = k\lambda/\beta\cos\theta$, where k is the shape factor with a typical value of 0.9, λ is the X-ray wavelength (0.154056 nm), β is the line broadening full width at half maximum (FWHM) peak height (in radians), and θ is the Bragg angle. Based on the peaks of Cu (111), Ag (111), Ag_3Sn (211) and Sn (200) planes, the mean sizes of Ag and Cu grains are calculated as 14.5 nm and 20.2 nm, respectively, both generally smaller than that of Ag_3Sn (44.0 nm) and Sn (57.6 nm) grains. This may be ascribed to the fact that the eutectic temperature of Ag-Cu alloy (1053 K) is higher than that of Ag-Sn alloy (753 K, 494 K) [24, 30]. The eutectic temperature of binary alloy is thought to be significant effect on the supply of growth species and subsequent nucleation/growth processes. The raw target is melted and evaporated into metal vapor which quickly spreads beyond the arc region, reaches a supersaturation state to form metal clusters as growth species and then generate bimetallic nanoparticles through cooling nucleation, growth and final condensation deposition. The alloy species with a low eutectic temperature are believed more likely to generate the accumulation of metal drop and develop a local liquid-rich regime that serves their sufficient nucleation and growth, as well as the generation of larger nanoparticles.

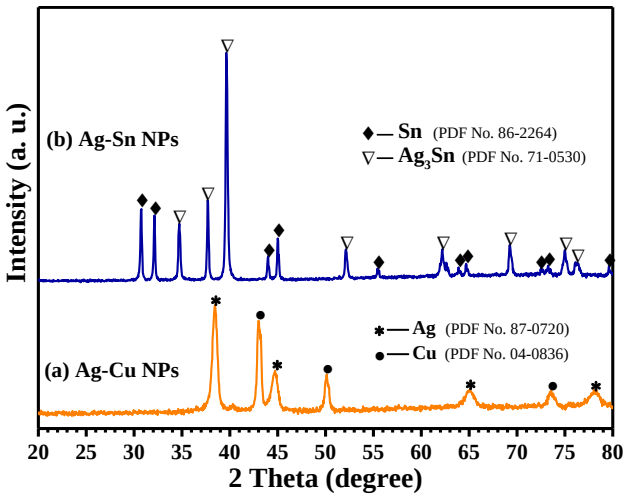

Fig. 1. XRD patterns of (a) Ag-Cu NPs and (b) Ag-Sn NPs.

The morphology and microstructure of the as-obtained nanoparticles were characterized by TEM and high-resolution TEM (HRTEM) as shown in Fig. 2. The TEM images in Figs. 2(a) and 2(b) show that all particles are essentially spherical in shape, with an average size of 33 nm for Ag-Cu NPs, and 64 nm for Ag-Sn NPs. HRTEM images of Figs. 2(a′) and 2(a″) further reveal that Ag-Cu NPs consist of separated Ag and Cu cores, both of which are encapsulated by amorphous oxide shells. The well-resolved lattice fringes of Ag and Cu cores correspond to the (111) crystal planes by variable spacing distances of 0.234 nm (FCC Ag) and 0.208 nm (FCC Cu). Figs. 2(b′) and (b″) show that Ag-Sn NPs are featured with the crystal cores of Ag_3Sn or Sn, and the tin oxides shells in a disordered state. The Ag_3Sn core is determined by an interplanar spacing of 0.224 nm belonging to the (211) planes, while the Sn core is confirmed by 0.278 nm of the lattice space between (101) crystal planes. The amorphous oxide shells are estimated about 1-4 nm in thickness, resulting from the nature of self-passivated process of the fresh nanoparticles. Herein, the oxygen-starved environment during passivation has caused the ultrathin layers of amorphous oxides. It can be also anticipated that Ag-Cu NPs are more active to be oxidized than Ag-Sn NPs, to be justified from the thicker oxide layers of Ag-Cu NPs. For this purpose, the further statistics evaluation on the thickness of their oxide layers was performed based on the HRTEM images, indicating an average thickness of 3.3 nm in range of 1.5-4.0 nm for Ag-Cu NPs and 2.4 nm in range of 2.0-2.5 nm for Ag-Sn NPs.

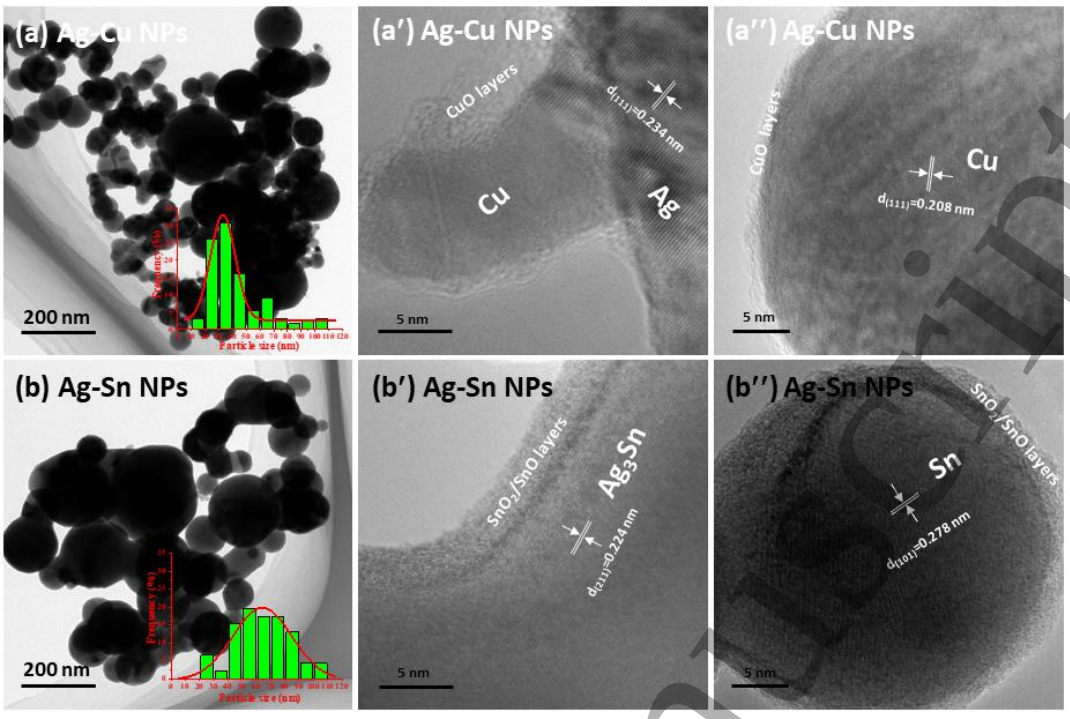

Fig. 2 TEM and HRTEM images of Ag-Cu NPs (a, a′, a″) and Ag-Sn NPs (b, b′, b″). The insets illustrate the size distribution of the nanoparticles based on the statistical analysis on TEM images.

XPS analysis was carried out to identify the surface oxides (shells) of the as-prepared nanoparticles as shown in Fig. 3. The survey spectra in Fig. 3(a) confirm the existence of Ag, Cu and O elements in Ag-Cu NPs, and Ag, Sn and O elements in Ag-Sn NPs. The contents of Ag, Cu and O in Ag-Cu NPs are detected as 40.9, 52.5, and 6.6 wt. %, while the Ag, Sn and O in Ag-Sn NPs are estimated as 38.3, 54.6 and 7.1 wt. %, respectively. The relative mass ratios are Ag/Cu = 43.8/56.2 and Ag/Sn = 41.2/58.8 for two kinds of the nanoparticles, both of which contain less Ag content with respect to the nominal composition of two raw targets (50/50 in mass ratio), implying a slight difference in elemental evaporation rates during the co-evaporation process. In Fig. 3(b), the spectrum of Ag 3d electrons for Ag-Cu NPs displays two peaks at 368.5 eV (Ag $3d_{5/2}$) and 374.5 eV (Ag $3d_{3/2}$), which is attributed to the Ag (Cu) solid solution core with zero-valence of Ag-Cu NPs, confirming the existence of Ag-based Ag(Cu) solid solution in the nanoparticles as indicated by the XRD result (Fig. 1). However, the binding energies positively shift by about 0.7-0.9 eV in comparison with that of pure Ag NPs [18, 31], which is in line with the behavior of previously reported bimetallic systems based on silver or platinum-group metals (PGMs) [32-35]. In the case of Ag-Sn NPs, Ag 3d electrons show the peaks at 368.3 eV (Ag $3d_{5/2}$) and 374.3 eV (Ag $3d_{3/2}$), and

both are from the intermetallic compound of Ag_3Sn [36]. Fig. 3(c) reveals the CuO shell of Ag-Cu NPs by the binding energies of Cu 2p electrons at 933.2 eV (Cu $2p_{3/2}$) and 953.0 eV (Cu $2p_{1/2}$), as well as the satellite signals of CuO (two characteristic bands in ranges of 940.6-947.7 eV and 959.7-965.2 eV). Meanwhile, two peaks at 932.6 eV (Cu $2p_{3/2}$) and 952.3 eV (Cu $2p_{1/2}$) verify the metallic Cu^0 state which is actually from the cores of Cu(Ag) solid solution in Ag-Cu NPs. The existence of CuO shell is also corroborated by the peak (529.9 eV) of O 1s electrons as illustrated in Fig. 3(d), where another peak at 531.0 eV is attributed to the physically absorbed oxygen and/or -OH groups [10, 18, 37]. Fig. 3(e) shows the signal of Sn 3d orbitals from Ag-Sn NPs. Two main peaks centred at 486.5 and 494.9 eV are assigned to SnO/SnO_2, and other two peaks at 484.6 and 493.1 eV are ascribed to the metallic Sn^0. In Fig. 3(f), O 1s spectrum shows overlapped peaks at 529.7 eV and 531.0 eV, both of which are from tin oxides, the shell of Ag-Sn NPs.

Above XPS analyses supply further evidence to the core-shell structures of the nanoparticles, i.e. the core of Ag(Cu)/Cu(Ag) solid solution and the shell of CuO layers in Ag-Cu NPs, while the core of Sn/Ag_3Sn grains and the shell of SnO/SnO_2 hybrid layers in Ag-Sn NPs. It is found that all bimetallic nanoparticles are coated by the layers of active metal (Cu and Sn) oxides, and no silver oxides have been detected. The reason is easier to understand that the Cu and Sn atoms at the surface of the nanoparticles have higher activity than Ag atoms; in consequence, they are preferentially oxidized by competing with Ag atoms to form the shells. It was also reported that the existence of electronic interaction between Ag and Cu/or Sn elements could render the counterpart of more active metals passive, thus in turn enhancing the resistance against oxidation of the bimetallic nanoparticles, which is similar to the case of Cu NPs grown on Au nanoislands [38]. It is well known that in microelectronic devices, the electrochemical migration of Ag component can cause a severe short-circuit failure in the presence of moisture and applied bias [39]. Hence, the oxides shells of Ag-based bimetallic nanoparticles are thought possible to prevent the diffusion and migration of Ag species, and therefore may contribute stable electrical conjunction.

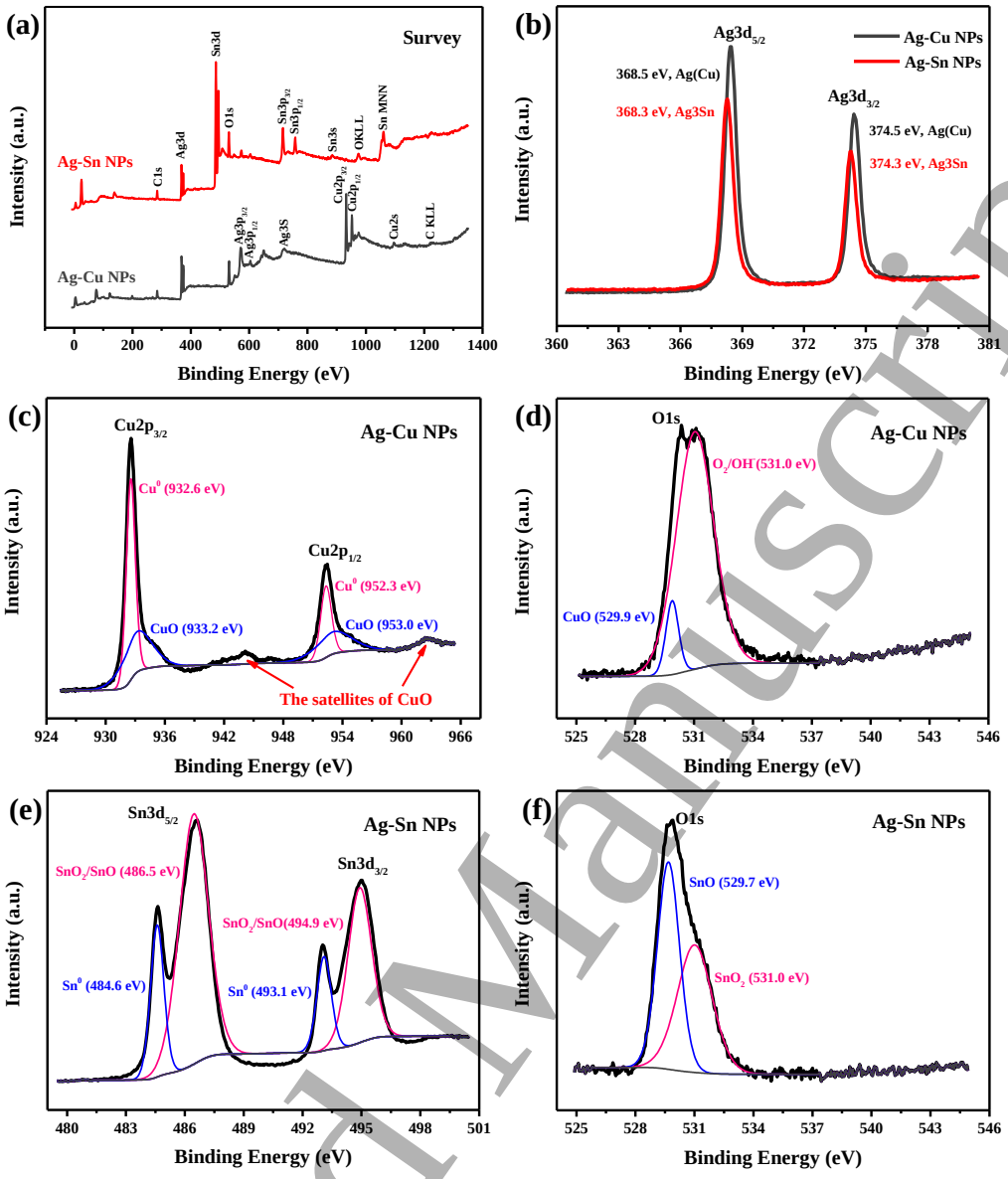

Fig. 3 XPS analysis on Ag-Cu NPs and Ag-Sn NPs. (a) Survey spectra; (b) The binding energies of Ag $3d_{5/2}$ and $Ag3d_{5/2}$ electrons of two kinds of nanoparticles; (c) and (d) The spectra of Cu 2p and O 1s electrons of Ag-Cu NPs, respectively; (e) and (f) The spectra of Sn 3d and O 1s electrons of Ag-Cu NPs, respectively.

Thermal stabilities of the as-prepared nanoparticles were measured in air by the simultaneous thermal analysis, as shown in Fig. 4. In Fig. 4(a), TGA curve of Ag-Cu NPs exhibits a slight weight loss of about 0.3 wt.% below 155 °C due to the volatilization of physisorbed moisture at surface of the nanoparticles, followed by a slow weight gain from 155 °C to 266 °C associated with a weak broadened exothermic peak of DSC curve centered at 204 °C, which might be attributed to the

oxidation of Cu core into Cu_2O [18]. A sharp exothermic peak occurs at 280 °C, yielding ~3 wt.% weight gain in the range of 266-300 °C, which is thought the further oxidation of Cu_2O into CuO [40]. As heating up to 750 °C, a successive weight gain without obvious thermal peaks implies complete oxidization from Cu to Cu_2O, and further to CuO, happened in Ag-Cu NPs. The total mass gain of Ag-Cu NPs in whole temperature range is about 13.1 wt.%, nearly close to the estimation based on XPS analysis, a mass gain of ~13.21 wt.% if the Cu core is entirely oxidized into CuO. The thermal behaviors of Ag-Cu NPs have well confirmed the existence of CuO shells and metallic cores in the nanoparticles. Fig. 4(b) presents TGA-DSC curves of Ag-Sn NPs, indicating an air-stable existence below 230 °C. The DSC curve shows the overlapped endo- and exo-thermal peaks along with a shoulder in the temperature range of 200-350 °C. Among them the endo-thermal reaction occurred at 221 °C corresponds to the melting of Sn component in Ag-Sn NPs, which is about 11 °C lower than the melting point (232 °C) of bulk Sn, plus a slight increase of 8 °C regarding to the reported eutectic temperature (207.3 °C) of $L \rightarrow \beta\text{-Sn} + Ag_3Sn$ in bimetallic Ag-Sn NPs (40 nm) [24, 26]. It is found that this endo-thermal sharp peak with a narrow width of ~6 °C implies a small size and its mono-size distribution of the Sn grains in the nanoparticles [41]. The prominent exothermic peak around 247 °C is considered the oxidation of molten Sn [4, 24, 27, 42, 43], while the shoulder near at 283 °C is from the further oxidizations of SnO products and the SnO shells [43]. The endothermic peak at 482 °C is thought as the melting of Ag_3Sn phase [27, 44], whereas an exothermic peak at 597 °C is ascribed to the oxidation of Sn produced by the decomposition of SnO [42] as well as the shoulder, supported by the sustaining weight gain, is due to the deep oxidation of SnO. Above thermal analysis results indicate that Ag-Sn NPs are more stable than Ag-Cu NPs in air below 200 °C, but suffer from the melting of Sn and Ag_3Sn components above 221 °C, and result in a breakage of the core/shell structure and further deep oxidizations. It is suggested that Ag-Cu NPs favor preserving the core/shell structure under high temperature sintering, through the protection from denser oxide layers. It had been proved that the fabrication of Ag-coated Cu@Ag core-shell NPs is also one of the most effective routes to protect them from oxidations, where Ag-Cu NPs are able to remain stable up to 200 °C [15, 45]. In the work, Ag-Cu NPs and Ag-Sn NPs are also air-stable up to 200 °C due to protection from the ultrathin oxides layers.

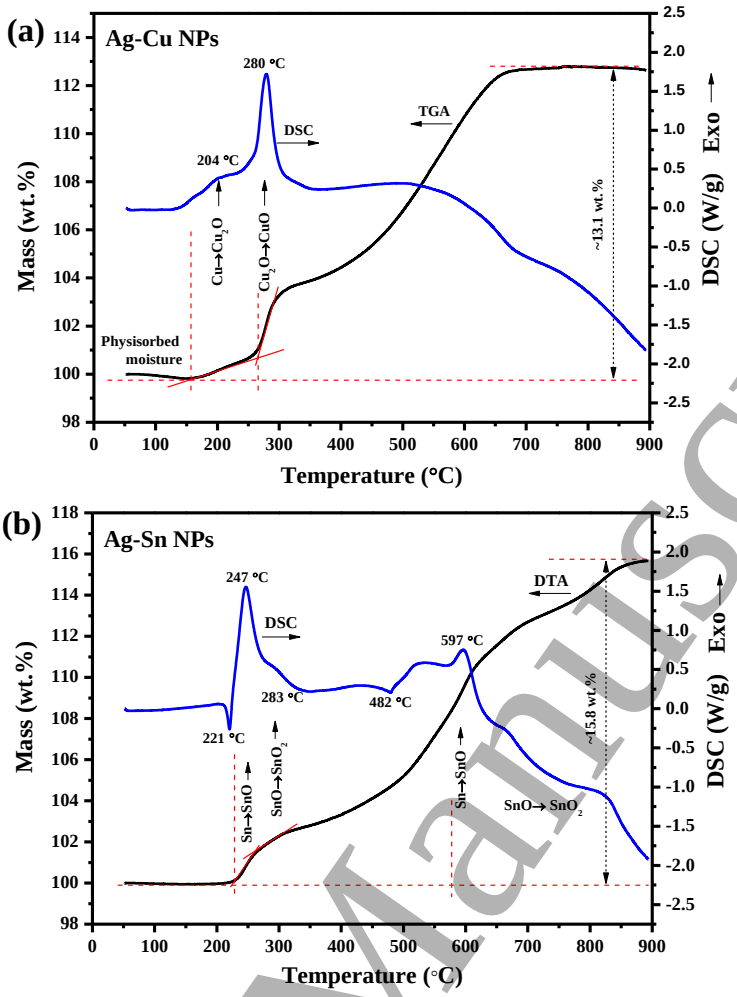

Fig. 4 TGA-DSC curves measured in air atmosphere. (a) Ag-Cu NPs, and (b) Ag-Sn NPs.

Fig. 5 demonstrates the relation between electrical resistivity of the nanoparticles and annealing temperature. It indicates that Ag-Sn NPs are generally better in electrical conductivity than Ag-Cu NPs regardless of annealing temperature. From the resistivity data of bulks, *i.e.* Sn (1.01×10^{-5} Ω·cm), Ag_3Sn (2.50×10^{-5} Ω·cm), Ag (1.59×10^{-6} Ω·cm) and Cu (1.72×10^{-6} Ω·cm) [46], one may recognize Ag-Sn NPs system would be higher in resistivity from the fact that it consists of main Ag_3Sn and Sn phases, while Ag-Cu NPs are comprised of Ag and Cu phases. Herein, the great influences from oxides layers (shells) could be expected on the electrical resistivity, that is, the CuO shells with an average thickness of 3.3 nm of Ag-Cu NPs are thicker and play more interference in comparison with the SnO/SnO_2 shells (2.4 nm) in Ag-Sn NPs. This estimation partly supported by the structural characterizations, and will be further proved by the temperature-dependent resistivity measurements in the following section. Ag-Cu NPs exhibit a room temperature resistivity of 7.10×10^{-5} Ω·cm, which is ~45% that of Cu NPs (1.58×10^{-4} Ω·cm), and ~17 times higher than that of Ag NPs

(3.94×10^{-6} Ω·cm); meanwhile Ag-Sn NPs are 4.24×10^{-5} Ω·cm in the resistivity, ~4 times lower than that of Sn NPs (2.04×10^{-4} Ω·cm) and one order higher than that Ag NPs or Ag nanowires (3.25×10^{-6} Ω·cm) [47].

The resistivity of all testing samples slightly decreases by raising the annealing temperature. It is believed that the annealing treatment can promote close contact between particles by metallurgic conjunction, and also reduce lattice defects by diffusion, consequently lower the resistivity of connected particles [1]. Especially, the melting of components in the nanoparticles can initiate the reconfiguration of nanostructures to create new conductive networks with a higher electrical conductivity [48]. For example, the melting of Sn grains in Ag-Sn NPs, as measured as 221 °C in Fig. 4(b), has harvested a remarkable decrease in the resistivity. Instead, Ag-Cu NPs show a gradual decrease in resistivity, owing to their ability to maintain the original core/shell structures up to a relatively higher temperature. Apparently, above results suggest the annealing process is favorable to get a well-established network with better conductivity, and present an optimal sintering temperature range for the bimetallic nanoparticles. It is worth to mention that the lowest resistivity, e.g. ρ = 6.96×10^{-5} Ω·cm of Ag-Cu NPs, 3.18×10^{-5} Ω·cm of Ag-Sn NPs, is quite comparable to the electrical performance (0.2~1.6 ×10^{-5} Ω·cm) of commercial Ag conductive inks [10]. It is expected that the bimetallic nanoparticles synthesized in this work have provided new opportunities for printed electronics.

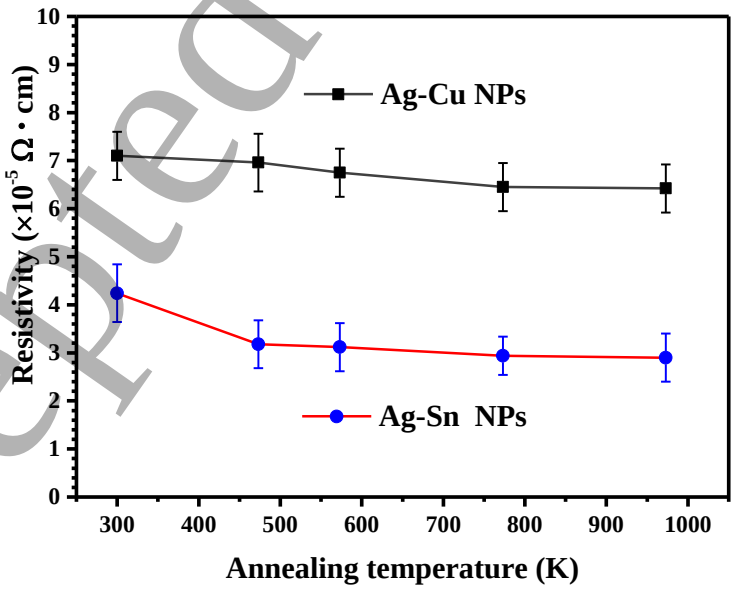

Fig. 5 Room-temperature resistivities of Ag-Cu NPs and Ag-Sn NPs versus the annealing temperature.

Temperature-dependent resistivity of Ag-Cu NPs and Ag-Sn NPs are presented in Figs. 6(a) and 6(b), respectively. In Fig. 6(a), Ag-Cu NPs demonstrate a typical metallic conduction behavior over 25 K with a positive temperature coefficient of resistance (TCR) but, nonetheless, a transition into dielectric behavior occurs at ~25 K. As revealed, the cores of Ag-Cu NPs consisting of metallic Ag(Cu) and Cu(Ag) solid solutions are attributed to the metallic behavior, while the thicker CuO shells are responsible for the dielectric activity at a low temperature. In the competition between conductive/dielectric domains, the circumambient temperature has crucial influences on the energic states of localized electrons and lattice phonons, as well as the interactions such as scattering, vibration and mobility [49]. The dominant metallic behavior is characterized by the electron-phonon scattering of crystal lattice [46], and the prevailing dielectric (the inset of Fig. 6a) can be understood from weak localization effects of electrons if the de-coherence length exceeds the shell thickness of CuO layer at low temperatures [50]. Fig. 6(b) shows a metallic behavior of Ag-Sn NPs, similar to the case of Ag-Cu NPs but determined by metallic Sn and Ag_3Sn phases. Additionally, a superconductive phenomenon is observed at 3.47 K as shown in the magnified inset of Fig. 6(b). It is believed that this superconductive behavior is arisen from the existence of Sn phase in Ag-Sn NPs, and the corresponding T_C (3.47 K) is very close to 3.72 K for the bulk tin [51]. In our previous work, the superconductive phenomenon was also found in Sn@CNT nanorods and T_C was determined as 3.69 K [52]. Above results verify the dominant metallic natures of both kinds of the nanoparticles at a higher temperature, even though they are completely coated by the dielectric layers of CuO or SnO/SnO_2.

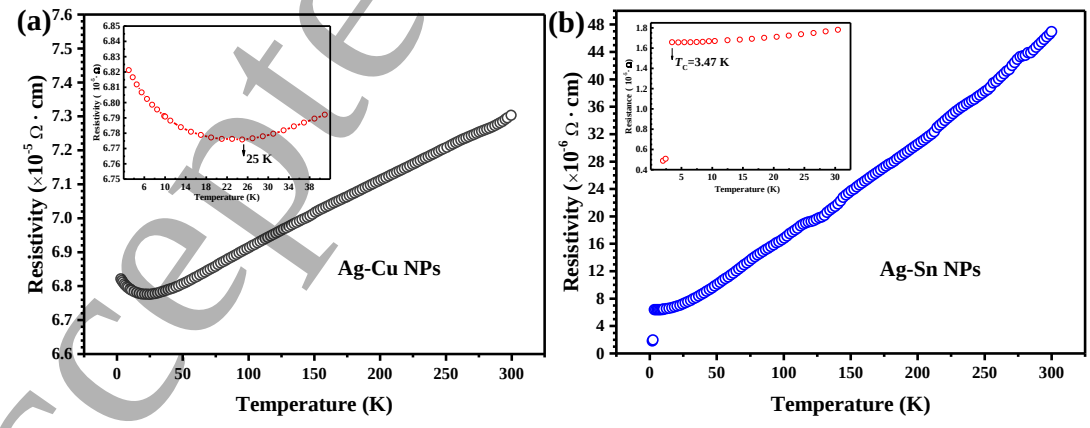

Fig. 6 Temperature dependence of resistivity of the testing sheets over 2-300 K. (a) Ag-Cu NPs and (b) Ag-Sn NPs. The inset of Fig. 6 (a) indicates a transition at 25 K from a dielectric to

metallic behavior, and the inset of Fig. 6 (b) shows a superconductive phenomenon below 3.47 K.

4. Conclusions

Ag-based bimetallic (Ag-Cu and Ag-Sn) NPs encapsulated by an ultrathin oxide shell have been successfully fabricated by DC arc-discharge method followed by a self-passivation process. The structural details of both bimetallic nanoparticles are experimentally confirmed as the metallic cores of Ag(Cu) and Cu(Ag) solid solutions for Ag-Cu NPs, and the crystal Ag and Ag_3Sn cores for Ag-Sn NPs. Surface analysis further confirms the CuO shell of Ag-Cu NPs and a hybrid (SnO/SnO_2) shell of Ag-Sn NPs. The bimetallic nanoparticles stable up to 200 °C in air exhibit a low resistivity, i.e. 7.10×10^{-5} Ω·cm for Ag-Cu NPs and 4.24×10^{-5} Ω·cm for Ag-Sn NPs. The unique core/shell structure of bimetallic nanoparticles makes them metallic and stabilized without a serious sacrifice of electrical conductivity. Both bimetallic nanoparticles demonstrate a typical metallic conduction behavior with a positive TCR over 25-300 K. Ag-Sn NPs exhibit a superconductive state below the metal-superconductor transition at T_C = 3.47 K. The bimetallic nanoparticles synthesized by this physical route have validated their competitive abilities in the thermal stability and electrical conductivity, making them the promising candidates of novel conducting materials for the flexible printed electronics.

Acknowledgements

This work was financially supported by the National Natural Science Foundation of China (NOs. 51331006 and 51271044).

References

[1] Kamyshny A and Magdassi S 2014 Conductive nanomaterials for printed electronics *Small* **10** 3515

[2] Singh M, Haverinen H M, Dhagat P and Jabbour G E 2010 Inkjet printing-process and its applications *Adv. Mater.* **22** 673

[3] Lee Y, Choi J R, Lee K J, Stott N E and Kim D 2008 Large-scale synthesis of copper nanoparticles by chemically controlled reduction for applications of inkjet-printed electronics *Nanotechnology* **19** 415604

[4] Jo Y H, Jung I, Kim N R and Lee H M 2012 Synthesis and characterization of highly conductive Sn-Ag bimetallic nanoparticles for printed electronics *J. Nanopart. Res.* **14** 782

[5] Park B K, Kim D, Jeong S, Moon J and Kim J S 2007 Direct writing of copper conductive

patterns by ink-jet printing *Thin Solid Films* **515** 7706

[6] Sirringhaus H, Kawase T, Friend R H, Shimoda T, Inbasekaran M, Wu W and Woo E P 2000 High-resolution inkjet printing of all-polymer transistor circuits *Science* **290** 2123

[7] Pajor-Świerzy A, Farraj Y, Kamyshny A and Magdassi S 2017 Air stable copper-silver core-shell submicron particles: Synthesis and conductive ink formulation *Colloid. Surface. A* **521** 272

[8] Park S, Vosguerichian M and Bao Z 2013 A review of fabrication and applications of carbon nanotube film-based flexible electronics *Nanoscale* **5** 1727

[9] Layani M, Kamyshny A and Magdassi S 2014 Transparent conductors composed of nanomaterials *Nanoscale* **6** 5581

[10] Lee C, Kim N R, Koo J, Lee Y J and Lee H M 2015 Cu-Ag core-shell nanoparticles with enhanced oxidation stability for printed electronics *Nanotechnology* **26** 455601

[11] Kamyshny A, Steinke J and Magdassi S 2011 Metal-based inkjet inks for printed electronics *Open Appl. Phys. J.* **4** 19

[12] Cummins G and Desmulliez M P Y 2012 Inkjet printing of conductive materials: a review *Circuit World* **38** 193

[13] Subramaniam C, Yamada T, Kobashi K, Sekiguchi A, Futaba D N, Yumura M and Hata K 2013 One hundred fold increase in current carrying capacity in a carbon nanotube-copper composite *Nat. Commun.* **4** 2202

[14] Brandes E A and Brook G B 1992 *Smithells metals reference book (Seventh edition)* (Oxford: Butterworth-Heinemann)

[15] Kim C K, Lee G-J, Lee M K and Rhee C K 2014 A novel method to prepare Cu@Ag core-shell nanoparticles for printed flexible electronics *Powder Technol.* **263** 1

[16] Tsai C Y, Chang W C, Chen G L, Chung C H, Liang J X, Ma W Y and Yang T N 2015 A study of the preparation and properties of antioxidative copper inks with high electrical conductivity *Nanoscale Res. Lett.* **10** 357

[17] Naoki T and Tetsu Y 1998 Bimetallic nanoparticles—novel materials for chemical and physical applications *New J. Chem.* **22** 1179

[18] Chen Z, Mochizuki D, Maitani M M and Wada Y 2013 Facile synthesis of bimetallic Cu-Ag nanoparticles under microwave irradiation and their oxidation resistance *Nanotechnology* **24** 265602

[19] Gao S, Huang H, Wu A M, Yu J Y, Gao J, Dong X L, Liu C J and Cao G Z 2016 Formation of Sn-M (M=Fe, Al, Ni) alloy nanoparticles by DC arc-discharge and their electrochemical properties as anodes for Li-ion batteries *J. Solid State Chem.* **242** 127

[20] Wang D X, Li D, Muhammad J, Zhou Y L, Shah A, Dong X L and Zhang Z D 2019 In situ synthesis of CNTs/Cu nanocomposites and the electronic transport properties *Phys. Status Solidi B* **256** 1800557

[21] Wang D, Li D, Muhammad J, Zhou Y, Wang Z, Lu S, Dong X and Zhang Z 2018 In situ synthesis and electronic transport of the carbon-coated Ag@C/MWCNT nanocomposite *RSC Adv.* **8** 7450

[22] Delogu F 2008 A mechanistic study of $Ag_{50}Cu_{50}$ solid solution formation by mechanical alloying *Acta Mater.* **56** 2344

[23] Ceylan A, Jastrzembski K and Shah S I 2006 Enhanced solubility Ag-Cu nanoparticles and their thermal transport properties *Metall. Mater. Trans. A* **37a** 2033

[24] Pinkas J, Sopoušek J, Brož P, Vykoukal V, Buršík J and Vřešťál J 2019 Synthesis, structure, stability and phase diagrams of selected bimetallic silver- and nickel-based nanoparticles *Calphad* **64** 139

[25] Okamoto H 2016 Supplemental literature review of binary phase diagrams: Ag-Li, Ag-Sn, Be-Pu, C-Mn, C-Si, Ca-Li, Cd-Pu, Cr-Ti, Cr-V, Cu-Li, La-Sc, and Li-Sc *J. Phase Equilib. Diffus.* **38** 70

[26] Sopousek J, Vrestal J, Zemanova A and Bursi J 2012 Phase diagram prediction and particle characterization of Sn-Ag nano alloy for low melting point lead-free solders *J. Min. Metall. Sect. B* **48** 419

[27] Sim K and Lee J 2014 Phase stability of Ag–Sn alloy nanoparticles *J. Alloys Compd.* **590** 140

[28] Zhang X F, Huang H and Dong X L 2013 Core/shell metal/heterogeneous oxide nanocapsules: The empirical formation law and tunable electromagnetic losses *J. Phys. Chem. C* **117** 8563

[29] Jenkins R and Snyder R L 1996 *Introduction to X-ray powder diffractometry* (New York: Wiley & Sons Inc.)

[30] Jabbareh M A and Monji F 2018 Thermodynamic modeling of Ag-Cu nanoalloy phase diagram *Calphad* **60** 208

[31] Ansari Z, Saha A, Singha S S and Sen K 2018 Phytomediated generation of Ag, CuO and Ag-Cu nanoparticles for dimethoate sensing *J. Photoch. Photobio. A* **367** 200

[32] Zhu Y X, Marianov A, Xu H M, Lang C and Jiang Y J 2018 Bimetallic Ag-Cu supported on graphitic carbon nitride nanotubes for improved visible-light photocatalytic hydrogen production *ACS Appl. Mater. Interfaces* **10** 9468

[33] Qian H, Chen S, Fu Y and Wang X 2015 Platinum–palladium bimetallic nanoparticles on graphitic carbon nitride modified carbon black: A highly electroactive and durable catalyst for electrooxidation of alcohols *J. Power Sources* **300** 41

[34] Li X, Park S and Popov B N 2010 Highly stable Pt and PtPd hybrid catalysts supported on a nitrogen-modified carbon composite for fuel cell application *J. Power Sources* **195** 445

[35] Luo M, Zhao Z, Zhang Y, Sun Y, Xing Y, Lv F, Yang Y, Zhang X, Hwang S, Qin Y, Ma J Y, Lin F, Su D, Lu G and Guo S 2019 PdMo bimetallene for oxygen reduction catalysis *Nature* **574** 81

[36] Luc W, Collins C, Wang S, Xin H, He K, Kang Y and Jiao F 2017 Ag-Sn bimetallic catalyst with a core-shell structure for CO2 reduction *J. Am. Chem. Soc.* **139** 1885

[37] Saikova S, Vorobyev S, Likhatski M, Romanchenko A, Erenburg S, Trubina S and Mikhlin Y 2012 X-ray photoelectron, Cu L3MM auger and X-ray absorption spectroscopic studies of Cu nanoparticles produced in aqueous solutions: The effect of sample preparation techniques *Appl. Surf. Sci.* **258** 8214

[38] Sohn Y, Pradhan D, Zhao L Y and Leung K T 2012 Anomalous oxidation resistance of "core-only" copper nanoparticles electrochemically grown on gold nanoislands prefunctionalized by 1,4-phenylene diisocyanide *Electrochem. Solid St.* **15** K35

[39] Li Y and Wong C P 2006 Monolayer protection for eletrochemical migration control in silver nanocomposite *Appl. Phys. Lett.* **89** 112112

[40] Yanase A and Komiyama H 1991 In situ observation of oxidation and reduction of small supported copper particles using optical absorption and X-ray diffraction *Surf. Sci.* **248** 11

[41] Dick K, Dhanasekaran T, Zhang Z Y and Meisel D 2002 Size-dependent melting of silica-encapsulated gold nanoparticles *J. Am. Chem. Soc.* **124** 2312

[42] Roshanghias A, Yakymovych A, Bernardi J and Ipser H 2015 Synthesis and thermal behavior of tin-based alloy (Sn-Ag-Cu) nanoparticles *Nanoscale* **7** 5843

[43] Song P X and Wen D S 2009 Experimental investigation of the oxidation of Tin nanoparticles *J. Phys. Chem. C* **113** 13470

[44] Yu F W, Wang B, Guo Q, Ma X, Li M Y and Chen H T 2018 Ag@Sn core-shell powder preform with a high re-melting temperature for high-temperature power devices packaging *Adv. Eng. Mater.* **20** 1700524

[45] Hai H T, Takamura H and Koike J 2013 Oxidation behavior of Cu-Ag core-shell particles for solar cell applications *J. Alloys Compd.* **564** 71

[46] Tian Y, Zhang Q M and Li Z Q 2011 Electrical transport properties of Ag3Sn compound *Solid State Commun.* **151** 1496

[47] Cheng Z, Liu L, Xu S, Lu M and Wang X 2015 Temperature dependence of electrical and thermal conduction in single silver nanowire *Sci. Rep-UK* **5** 10718

[48] Liu X J, Zheng Z, Wang C Q, Liu W and Kong L C 2016 Effects of temperature and dispersants on the phases and morphology of Ag-Cu nanoparticles *J. Mater. Sci-Mater. El.* **27** 10065

[49] Bai G H, Wu C, Jin J Y and Yan M 2016 Structural, electron transportation and magnetic behavior transition of metastable FeAlO granular films *Sci. Rep-UK* **6** 24410

[50] Beloborodov I S, Glatz A and Vinokur V M 2007 Electron transport in nanogranular ferromagnets *Phys. Rev. Lett.* **99** 066602

[51] Hung C-H, Lee C-H, Hsu C-K, Li C-Y, Karna S K, Wang C-W, Wu C-M and Li W-H 2013 Unusually large magnetic moments in the normal state and superconducting state of Sn nanoparticles *J. Nanopart. Res.* **15** 1905

[52] Wang D X, Li D, Muhammad J, Zhou Y L, Zhang X F, Wang Z M, Lu S S, Dong X L and Zhang Z D 2018 Buildup of Sn@CNT nanorods by in-situ thermal plasma and the electronic transport behaviors *Sci. China Mater.* **61** 1605